The Neupert Effect of Flare Ultraviolet and Soft X-Ray Emissions

Jiong Qiu

Qiu, J. (2021). The Neupert effect of flare ultraviolet and soft X-ray emissions. The Astrophysical Journal, 909(2), 99.

The Astrophysical Journal, 909:99 (14pp), 2021 March 10 https://doi.org/10.3847/1538-4357/abe0b3

The Neupert Effect of Flare Ultraviolet and Soft X-Ray Emissions

Jiong Qiu
Department of Physics, Montana State University, Bozeman, MT, USA
Received 2020 August 22; revised 2021 January 26; accepted 2021 January 26; published 2021 March 10

Abstract

We model the Neupert effect that relates flare heating energy with the observed soft X-ray (SXR) emission. The traditional form of the Neupert effect refers to the correlation between the time-integrated hard X-ray or microwave light curve and the SXR light curve. In this paper, we instead use as the proxy for heating energy the ultraviolet (UV) emission at the footpoints of flare loops and modify the model of the Neupert effect by taking into account the discrete nature of flare heating, as well as cooling. In the modified empirical model, spatially resolved UV light curves from the transition region or upper chromosphere are each convolved with a kernel function characterizing the decay of the flare loop emission. Contributions by all loops are summed to compare with the observed total SXR emission. The model has successfully reproduced the observed SXR emission from its rise to decay. To estimate the heating energies in flare loops, we also employ the UV footpoint calorimeter (UFC) method that infers heating rates in flare loops from these UV light curves and models the evolution of flare loops with a zero-dimensional hydrodynamic code. The experiments show that a multitude of impulsive heating events do not well reproduce the observed flare SXR light curve, but a two-phase heating model leads to better agreement with observations. Comparison of the two models of the Neupert effect further allows us to calibrate the UFC method and improve the estimate of heating rates in flare loops continuously formed by magnetic reconnection throughout the flare evolution.

Unified Astronomy Thesaurus concepts: Solar ultraviolet emission (1533); Solar x-ray emission (1536); Solar flares (1496); Solar magnetic reconnection (1504)

1. Introduction

Neupert (1968) discovered that the time integral of the microwave light curve of a flare is correlated with the flare soft X-ray (SXR) light curve during its rise. Subsequently, the Neupert effect has been confirmed in generations of flare observations. Dennis & Zarro (1993) studied 66 flares observed in 1980 by the Hard X-ray Burst Spectrometer on the Solar Maximum Mission (Orwig et al. 1980) and the Geostationary Operational Environmental Satellite (GOES), finding that 80% of large flares exhibit good correlations between the hard X-ray (HXR) light curve and the time derivative of the GOES SXR light curve in the 1–8 Å passband. Applying the time correlation analysis to more than 1000 flares observed between 1997 January and 2000 June by GOES and the Burst and Transient Source Experiment on board the Compton Gamma-Ray Observatory (Schwartz et al. 1992), Veronig et al. (2002) confirmed that the timing behavior of the HXR and SXR emissions in large flares is consistent with the Neupert effect. McTiernan et al. (1999) examined flare SXR and HXR observations by the Soft X-ray Telescope (Tsuneta et al. 1991), the Bragg Crystal Spectrometer (Culhane et al. 1991), and the Hard X-ray Telescope (Kosugi et al. 1991) on Yohkoh, finding the Neupert effect more prominently demonstrated in high-temperature SXR light curves. Effenberger et al. (2017) further confirmed the Neupert effect exploiting flare observations by RHESSI (Lin et al. 2002) for the past two solar cycles. The Neupert effect has also been found in small flares. Qiu et al. (2004a) studied the Neupert effect in more than 100 microflares (of GOES class A–C1) with significant HXR emissions observed by RHESSI, finding that the time derivative of the GOES SXR emission is best correlated with the HXR emission at the photon energy 14–20 keV. Glesener et al. (2020) recently detected nonthermal HXR emission in a A5.7 microflare observed by the Nuclear Spectroscopic Telescope Array (Grefenstette et al. 2016), which also exhibits the Neupert effect.

The Neupert effect is interpreted as flare plasmas in the corona being heated by nonthermal electrons. These electrons precipitate at the lower atmosphere and lose their energy instantaneously by collision with ions. In this course, thick-target HXR emissions are generated, and chromosphere evaporation is driven that heats the corona as well as increases the density of the corona, leading to the enhanced SXR emission (e.g., Antonucci et al. 1982; Fisher et al. 1985; Li et al. 1993; Lee et al. 1995). Therefore, the HXR light curve of a flare can serve as the proxy of the electron energy flux, and its time integral is equivalent to the maximum thermal energy of the subsequently heated flare plasmas in the corona, achieved at the time when the flare SXR emission peaks. Analyzing spectroscopic observations of flares, a number of studies have then estimated this maximum flare thermal energy, as well as the total energy in nonthermal electrons, suggesting that these two energies are indeed comparable in large flares (see Emslie et al. 2012; Aschwanden et al. 2017, and references therein), and sometimes in small flares as well (e.g., Glesener et al. 2020). With this notion, generations of hydrodynamic models have been developed to study the evolution of the flare corona with nonthermal electron beams as the primary source of heating (Somov et al. 1981; Nagai & Emslie 1984; Mariska et al. 1989; Emslie et al. 1992; Warren & Antiochos 2004; Reep 2014). Specifically, effort has been made to model the evolution of the flare corona (and chromosphere) using observed HXR light curves or the time derivative of SXR light curves to infer time-dependent heating rates in flares and reproduce the observed thermodynamic properties of flare plasmas in the corona and chromosphere (Fisher & Hawley 1990; Rubio da Costa et al. 2016).

Despite the prevailing evidence in support of the Neupert effect, there are several caveats in the traditional form of the Neupert effect. It only addresses the rise phase of the flare SXR

emission and only considers nonthermal electrons as the primary carrier of corona heating energy. As has been noted for decades, energy release and flare heating often continue into the decay phase of the flare SXR emission, when the HXR emission has usually diminished, and the amount of heating energy deposited in the decay phase can be significant (Withbroe 1978; Dere & Cook 1979; Ryan et al. 2013). Whereas prior studies have confirmed the Neupert effect in a large number of flares, these same studies have also revealed that, in a significant fraction of flares, the SXR emission continues to rise after the HXR emission has ended (Veronig et al. 2002), and in some flares, the SXR emission rises before the HXR emission (Effenberger et al. 2017). These observations indicate that other sources of energy are needed to heat the flare corona (Veronig et al. 2005). Furthermore, flare heating takes place in many flare loops that are generated continuously into the decay phase. These loops are heated by chromosphere evaporation driven by either nonthermal beams or something else, such as thermal conduction (Gan et al. 1991; Longcope 2014) or Alfvén waves (Fletcher & Hudson 2008; Kerr et al. 2016), and then cool, and the total SXR emission at any given time is the sum of the emissions from all of these loops at their different evolution stages (e.g., Aschwanden & Alexander 2001). The continuous heating and cooling of multiple flare loops cannot be well described by the Neupert effect applied to the total HXR and SXR emissions that are not spatially resolved.

These questions motivate the thinking to extend the Neupert effect to a broader context that addresses the nature of flare heating on elementary scales and perhaps beyond nonthermal electrons. Apart from microwave and HXR light curves, which are indicative of nonthermal electrons, flare emission in the lower atmosphere observed in the optical, ultraviolet, and extreme-ultraviolet (EUV) wavelengths generally exhibits an impulsive behavior before the more gradual rise of the SXR emission (see the review by Fletcher et al. 2011). In large flares, enhanced UV and EUV emissions have often been found to trace HXR emissions temporally and/or spatially (Kane & Donnelly 1971; McClymont & Canfield 1986; Cheng et al. 1988, 2012; Cheng 1990; Fletcher & Hudson 2001; Warren & Warshall 2001; Qiu et al. 2010), supporting the scenario of heating by nonthermal electrons. But observations have also shown impulsive UV emissions at the flare footpoints not associated with thick-target HXR signatures (Warren & Warshall 2001; Alexander & Coyner 2006; Coyner & Alexander 2009; Cheng et al. 2012), and in these cases, it is likely that the temperature of the corona is rapidly raised, and thermal conduction would deposit energy at the chromosphere, causing enhanced optical, UV, and EUV emissions and driving chromosphere evaporation as well. Most recently, spectroscopic observations in these wavelengths with high spatial resolutions have revealed downflows (chromosphere condensation) and upflows (chromosphere evaporation) in a large number of flare kernels at unprecedented small scales, illustrative of prototypical elementary energy release events in the flare (Graham & Cauzzi 2015). These state-of-the-art observations clearly demonstrate the critical role of chromosphere evaporation in energizing the flare corona regardless of heating mechanisms.

The advanced flare observations in the lower atmosphere provide us with the opportunity to better characterize heating rates in flare loops. In this spirit, we analyze the ultraviolet emission from the transition region and upper chromosphere at the footpoints of flare loops. The transition region and upper chromosphere respond promptly to energy release in the corona, and the resultant UV emission can be used as a proxy for heating. This approach is free from the assumption that heating is primarily by nonthermal electrons. Furthermore, high-resolution UV images allow us to track flare loops that are formed and heated at different times and evolve independently throughout the flare, assuming that these loops are anchored at brightened UV pixels. This paper presents a thought experiment on the Neupert effect using spatially resolved UV light curves instead of HXR light curves and with two models, a modified empirical model of the Neupert effect and the UV footpoint calorimeter (UFC) method that infers heating rates from UV light curves and models the evolution of the flare corona in a multitude of loops (Qiu et al. 2012; Liu et al. 2013). Both models take into account heating as well as cooling of flare loops formed at different times during the flare, which contribute to the observed total SXR emission. The first model examines the temporal relationship between the SXR and spatially resolved UV 1600 Å light curves but cannot return the heating energy, whereas the UFC method will be able to infer the heating rates in flare loops. In this study, we analyze 16 flares observed by GOES and the Atmospheric Imaging Assembly (AIA; Lemen et al. 2012; Section 2), apply the empirical model (Section 3) and UFC method (Section 4) to these flares to reproduce the GOES SXR light curves, and improve the estimate of flare heating energies by comparing these two models (Section 5). Conclusions and discussions are given in the last section.

2. Flare Light Curves

We have analyzed 16 flares listed in Table 1. The flare SXR emissions were obtained by GOES,[1] and imaging observations of the flares in the UV 1600 Å passband were obtained by AIA on board the Solar Dynamics Observatory (SDO; Pesnell et al. 2012). Except for one event, SOL 2011-12-26 (event 3), these flares were also observed by RHESSI. Table 1 presents the information on the source region and position of each flare, the duration of the flare τ_d derived from the flare light curves, and the median half-length of the flare loops estimated from the separation of the flare ribbons observed in the AIA 1600 Å images. The magnetic flux enclosed in the total area of the flare ribbons gives the measurement of the total reconnection flux $\Phi_{\rm rec}$ (e.g., Qiu et al. 2004b; Saba et al. 2006), and the uncertainty in $\Phi_{\rm rec}$ is characterized by the difference in the magnetic flux measured in positive and negative magnetic fields, respectively. The total heating energy and its uncertainty in each flare are derived in the following text (Sections 3, 4, and 5.1).

Figure 1 shows the light curves of each of the 16 flares, including the GOES SXR light curve at 1–8 Å (denoted as $\mathcal{F}_{\rm sxr}$, in units of W m^{-2}, in the following text), its time derivative ($\dot{\mathcal{F}}_{\rm sxr}$), the total count-rate light curve in the UV 1600 Å passband integrated over the flare region ($\mathcal{F}_{\rm uv}$, in units of DN

[1] In the table, the magnitude of the flare is based on the GOES flux in the 1–8 Å passband, which has historically been scaled to match the flux by GOES satellites 1–7. As of 2020 October 28, the SXR flux obtained by GOES satellites 8–15 was reported as the "true" flux, which is equivalent to the "scaled" flux divided by 0.7 for the long channel (1–8 Å) and 0.85 for the short channel (0.5–4 Å), respectively (https://hesperia.gsfc.nasa.gov/rhessidatacenter/complementary_data/goes.html). The flares analyzed in this paper were observed by GOES satellites 10–15, and analysis in this paper uses the "true" flux in units of W m^{-2}; however, to be consistent with the past literature, the flare magnitude reported in Table 1 is still derived using the "scaled" flux.

Table 1
Properties of Flares and Model Parameters

	Start Time, Magnitude[a]	Position	τ_d (minutes)[b]	L (Mm)[c]	Φ_{rec} (10^{20} Mx)[d]	$\mathcal{E}_{tot}$ (10^{30} erg)[e]	Cross-correlation Coefficient and Time Lag (s)[f]		
							12–25 keV	25–50 keV	UV1600
1	2005-05-13 16:33 M8.0	NOAA10759 N12E05	62	43 (23)	76.2 (5.5)	34.6 (7.8)	0.41 (0)	0.88 (20)	0.79 (0)
2	2011-04-22 04:26 M1.8	NOAA11195 S17E29	64	29 (6)	15.2 (6.3)	11.3 (4.8)	0.71 (−33)	0.64 (8)	0.72 (0)
3	2011-12-26 11:16 C5.1	NOAA11384 N13W14	160	35 (5)	5.8 (0.1)	7.5 (1.5)	⋯	⋯	0.65 (−100)
4	2013-08-12 10:25 M1.5	NOAA11817 S22E10	35	9 (0)	8.7 (3.5)	3.6 (0.9)	0.91 (−20)	0.91 (14)	0.89 (−40)
5	2013-08-30 01:58 C8.0	NOAA11836 N12E28	150	76 (53)	8.9 (0.9)	11.9 (0.6)	0.76 (0)	0.53 (208)	0.74 (−120)
6	2014-02-05 18:33 C7.1	NOAA11967 S12W36	34	14 (3)	5.2 (0.6)	2.3 (0.8)	0.93 (0)	0.44 (137)	0.81 (0)
7	2014-04-18 12:38 M7.2	NOAA12036 S15W42	55	31 (13)	20.6 (3.0)	26.8 (5.9)	⋯	⋯	0.70 (−100)
8	2014-05-10 06:52 C7.7	NOAA12056 N04E17	24	18 (6)	8.5 (0.4)	3.6 (0.9)	0.92 (0)	0.88 (0)	0.82 (−60)
9	2014-06-15 23:30 C9.0	NOAA12087 S18W11	66	15 (6)	6.5 (0.9)	5.4 (0.5)	0.90 (−41)	0.85 (127)	0.93 (−20)
10	2014-09-28 02:41 M5.0	NOAA12173 S21W24	52	28 (3)	15.9 (0.6)	17.6 (5.0)	0.72 (−39)	0.67 (98)	0.72 (0)
11	2014-11-09 15:26 M2.3	NOAA12205 N15E05	16	7 (35)	9.3 (1.5)	3.9 (1.0)	⋯	⋯	0.77 (−20)
12	2014-12-01 06:28 M1.8	NOAA12222 S20E04	32	25 (6)	9.5 (1.1)	5.4 (1.4)	0.85 (−8)	0.77 (49)	0.91 (0)
13	2014-12-04 18:02 M6.2	NOAA12222 S20W35	45	28 (15)	26.4 (4.0)	25.4 (7.2)	0.79 (−155)	0.85 (0)	0.89(−20)
14	2014-12-17 14:42 C9.3	NOAA12242 S19W02	25	7 (9)	4.7 (0.1)	1.1 (0.1)	0.95 (−24)	0.98 (10)	0.96 (−20)
15	2014-12-17 18:56 M1.4	NOAA12241 S10E17	14	9 (10)	8.1 (4.1)	3.0 (0.8)	0.37 (−94)	0.89 (0)	0.73 (−20)
16	2014-12-19 09:33 M1.2	NOAA12237 S13W40	30	16 (5)	6.9 (2.7)	5.0 (1.8)	0.69 (0)	0.35 (12)	0.71 (0)

Notes.
[a] Flare magnitude is based on the "scaled" GOES SXR flux in 1–8 Å but not the "true" flux released in 2020 October. Determination of the start time t_s is described in the text (Section 2).
[b] The duration of the flare, $\tau_d = t_e - t_s$, where t_s and t_e are start and end times defined in the text (Section 2).
[c] The median length of flare half-loops. Also shown in parentheses is the standard deviation of the length of the loop events, which grows as the flare evolves (see text in Section 4).
[d] The total reconnection flux measured from flare ribbon pixels with brightness at least four times the quiescent background for at least 4 minutes; given in parentheses is the difference in the magnetic flux measured in positive and negative magnetic fields, respectively (Section 5.2).
[e] Total heating energy of the flare corona, which is the mean of $\sum\mathcal{E}_{UFC}$ and $\sum\mathcal{E}_{emp}$; the difference between $\sum\mathcal{E}_{UFC}$ and $\sum\mathcal{E}_{emp}$ is given in parentheses (see Section 5.1).
[f] The maximum coefficient of the time-lagged cross-correlation between two light curves, one being the time derivative of the GOES SXR 1–8 Å light curve and the other being the HXR count-rate light curve in 12–25 keV, in 25–50 keV by RHESSI, or the total UV 1600 Å count flux by AIA. A positive time lag indicates that the time derivative of the SXR light curve lags other light curves. The correlation with HXR light curves is not available for events 3, 7, and 11 due to a lack of RHESSI observations from the start of the flare.

s^{-1}), and the HXR count-rate light curve of photon energy 12–25 keV by RHESSI. Following the convention, here we refer to the time period before the peak of the SXR 1–8 Å light curve as the rise phase, or the impulsive phase, of a flare, followed by the gradual phase, or the decay phase.

Most of these flares exhibit the well-known Neupert effect, namely, the flare HXR light curve is temporally correlated with the time derivative of the 1–8 Å SXR light curve $\dot{\mathcal{F}}_{sxr}$ during the rise of the SXR emission. To examine the degree to which the Neupert effect applies, we conduct a time-lagged cross-correlation between $\dot{\mathcal{F}}_{sxr}$ and the HXR light curves at 12–25 and 25–50 keV, respectively, and the derived maximum cross-correlation coefficients and time lags are given in Table 1. In a few flares, the HXR emission in 12–25 keV lags $\dot{\mathcal{F}}_{sxr}$ by within a minute, likely due to the mixture of thermal emission in this channel (e.g., Veronig et al. 2005; McAteer & Bloomfield 2013). In comparison, the HXR emission in 25–50 keV (not shown in the figure) does not lag $\dot{\mathcal{F}}_{sxr}$. Since most of these flares do not exhibit significant HXR emissions beyond 25 keV, here we do not conduct a comprehensive energy-dependent analysis (e.g., McAteer & Bloomfield 2013); instead, this study focuses on flare UV light curves in the AIA 1600 Å passband.

Readers are reminded that, throughout the following text, the flare UV light curve, $\mathcal{F}_{uv}$, specifically refers to emission in the AIA 1600 Å passband. The flare emission in this passband is dominated by C IV, Si II, C I, and He II lines formed in the transition region and the upper chromosphere in the temperature range $4.2 < \log T < 5.1$ (Simões et al. 2019). Using high-resolution spectral observations by the Skylab during the decay phase of a flare, Simões et al. (2019) found that the most notable line, the C IV line (100,000 K) in this passband, contributes to 26% of the AIA 1600 Å flare emission. Figure 1 shows that $\mathcal{F}_{uv}$ matches $\dot{\mathcal{F}}_{sxr}$ very well during the rise phase, and the coefficients of the cross-correlation and time lags between the two are similar to those between $\dot{\mathcal{F}}_{sxr}$ and the HXR 12–25 keV emission, suggesting a close relation between the HXR emission and the transition region and upper chromosphere line emission (e.g., Cheng et al. 1984), such as the emission in the AIA 1600 Å passband analyzed in this study. On the other hand, it is noted that the flare UV emission at this passband proceeds for a longer time than both the $\dot{\mathcal{F}}_{sxr}$ and HXR light curves.

The flare emission in the AIA 1600 Å passband is produced by heating of the transition region or upper chromosphere with reconnection released energy carried along newly formed flare loops into the lower atmosphere at their feet. Figure 2 shows, as examples, two flares, SOL 2014-04-18 (event 7) and SOL 2013-08-12 (event 4). The left panels show the evolution of flare ribbons in the UV 1600 Å passband mapped on a line-of-sight magnetogram obtained from the Helioseismic and Magnetic Imager (HMI; Schou et al. 2012). The color code indicates the earliest time a pixel is brightened or its activation time, defined as the time when its brightness reaches four times

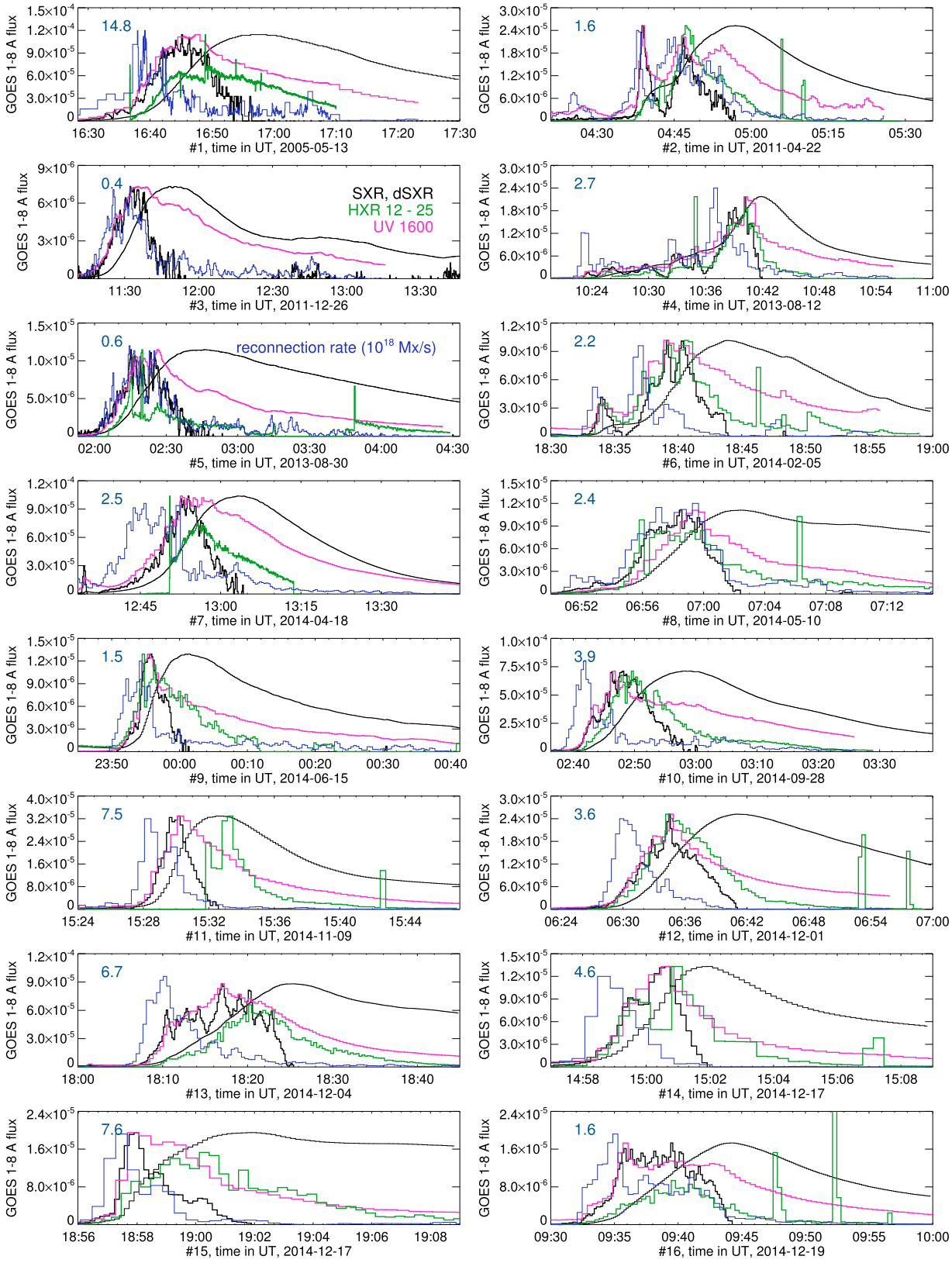

Figure 1. Light curves of the flares analyzed and modeled in this paper. These include the GOES SXR "true" flux in 1–8 Å in units of W m^{-2} and its time derivative (black); the total UV count-rate light curve (pink), integrated over the flare region in the 1600 Å passband from AIA/SDO; and the HXR count-rate light curve (green) at the photon energy 12–25 keV observed by RHESSI. Also plotted is the time profile of the reconnection rate in units of 10^{18} Mx s^{-1} (blue), with the peak reconnection rate marked in each panel. Except for the SXR light curve, all other light curves are arbitrarily scaled. For clarity of the display, the uncertainties in the reconnection rates are not plotted, but they are described in the text (Section 5.2).

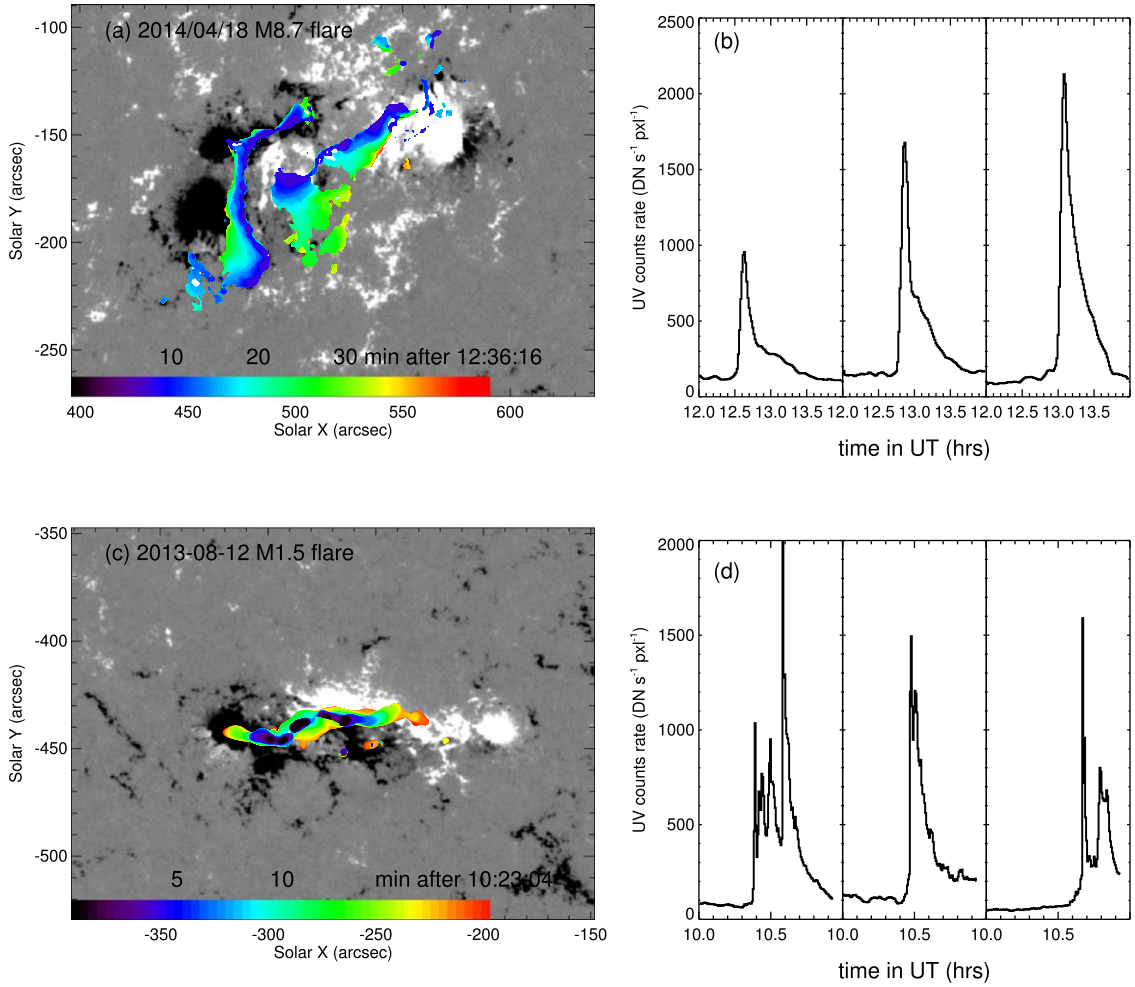

Figure 2. Left: evolution of flare ribbon brightening in UV 1600 Å passband superimposed on a line-of-sight magnetogram, obtained by HMI, for flare 7 SOL 2014-04-18 (a) and flare 4 SOL 2013-08-12 (c). For display, the magnetogram is saturated at ±300 G. The color code indicates the time of the start of the flare brightening defined as when the brightness is four times the brightness of the preflare quiescent background. Right: UV 1600 Å light curves in a few brightened pixels, showing that flare energy release takes place in different places (loops) at different times and proceeds into the decay phase of the flare SXR emission.

the preflare quiescent background (Qiu et al. 2010). The right panels show the UV 1600 Å light curves from a few brightened pixels during the flare. From these figures, it is evident that, after the impulsive phase of a flare, reconnection continues to form flare loops and releases energy in them, and the continuous reconnection into the decay phase contributes to the prolonged total UV emission. These observations suggest that spatially resolved flare light curves of UV or optical emission in the lower atmosphere provide comprehensive temporal coverage and spatial mapping of reconnection energy release events in a flare. Therefore, in this study, we use the flare UV 1600 Å emission as the proxy for flare heating regardless of the heating mechanism. We examine the Neupert effect that relates spatially resolved UV light curves with the total SXR light curve and estimate the heating energies in flare loops assumed to be anchored at the UV-brightened pixels.

For this purpose, we obtain spatially resolved UV 1600 Å light curves in flaring pixels whose brightness is increased to at least four times the quiescent background and stays bright for at least 4 minutes. The first criterion is used to distinguish flaring pixels from plages, whose brightness distribution peaks at 3.5 times the quiescent background. The second criterion helps to pick out pixels at the feet of closed loops, different from the feet of open field lines or ejecta, which are brightened only briefly. For each of the flares in Table 1, a few thousand flaring pixels are identified. We assume that anchored to each UV-bright pixel is a flaring half-loop, and the UV brightness at the pixel is somewhat scaled to the heating flux in the half-loop. In the foregoing text, each of these half-loops is called a loop event, or a heating event. We then use two methods, an empirical formula of the Neupert effect and a zero-dimensional hydrodynamic code, to model these heating events and reproduce the synthetic SXR light curve $\mathcal{F}_{\rm sxr}$ comparable with GOES observations.

We specify the time range for the analysis of the UV 1600 Å and SXR light curves. The start time t_s of a flare is defined as when $\mathcal{F}_{\rm sxr}$ rises to e^{-4} of its peak emission. The end time of the flare t_e is defined by $\mathcal{F}_{\rm uv}$, instead, as when $\mathcal{F}_{\rm uv}$ decays to e^{-2} of its maximum. The duration of the flare is $\tau_d = t_e - t_s$ and reported in Table 1.

3. Neupert Effect: An Empirical Model

The Neupert effect refers to the observation that the time-integrated HXR or microwave light curve matches the SXR light curve from its rise to peak. The SXR emission then decays because of the reduced emissivity in the passband due to decreased temperature (cooling) and/or density, which is not

addressed by the Neupert effect in its original form. Furthermore, during a flare, numerous flare loops are formed and heated and then cool at different times. The total SXR emission at any given time is the sum of the emissions from these loops, each at its own distinct evolution stage; earlier formed flare loops may be cooling during the rise of $\mathcal{F}_{\rm sxr}$, whereas new heating events may still take place when $\mathcal{F}_{\rm sxr}$ appears to decay.

To model the Neupert effect in its complete form, we take into consideration the discrete nature of flare heating, as well as cooling in individual flare loops, and compare the sum of the flare emission from multiple loops with the observed total SXR emission. We assume that each newly brightened UV pixel is the foot of a newly formed flare half-loop, and the UV light curve of the pixel is simply scaled to the heating rate in the loop event. We then convolve the UV light curve of each loop event with a kernel function $\mathcal{K}$ that represents the decay of the flare emission in the loop. The modeled total SXR emission is therefore given by

$$\mathcal{F}_{\rm sxr}(t) = c_0 \sum_{i=1}^{N} \int_0^t \mathcal{F}_{{\rm uv},i}(t')\mathcal{K}_i(t, t')dt', \quad (1)$$

where subscript i indicates the contribution from the ith loop event, assumed to be anchored to the ith UV-brightened pixel, and c_0 is a scaling constant relating SXR and UV emissions. We have experimented with several forms of the kernel function and found that the function of a half Gaussian provides the best model,

$$\mathcal{K}_i(t, t') = \exp\left[\frac{-(t-t')^2}{2\tau_i^2}\right](t > t'), \quad (2)$$

where τ_i is the decay timescale of the emission of the ith loop event. When $\tau_i \to \infty$, Equation (1) gives the traditional description of the Neupert effect, that $\mathcal{F}_{\rm sxr}$ is the time integral of $\mathcal{F}_{\rm uv}$ without taking cooling into account.

An automated routine is run to search for the optimal decay timescale τ_i so that the model light curve $\mathcal{F}_{\rm sxr}$ matches the observed light curve. Our experiments suggest that Equation (1) with the same constant τ_i for all loop events cannot reproduce the observed $\mathcal{F}_{\rm sxr}$ from rise to decay. We then allow the decay time τ_i to be time-dependent, considering that, as the flare evolves, reconnection takes place at higher altitudes producing longer loops, which take a longer time to cool. For a given flare, we use the following trial function to determine τ_i:

$$\tau_i = \tau_0 \exp\left[\frac{t_i - t_s}{f\tau_d}\right]. \quad (3)$$

Here t_i is the peak time of $\mathcal{F}_{{\rm uv},i}$ for the ith loop event, t_s and t_e are the start and end times of the flare previously defined, and $\tau_d \equiv t_e - t_s$ is the duration of the flare. For each loop event, τ_i is constant. For each flare, τ_0 and f are constant, which gives the decay time at the start of the flare and the growth rate of the decay time as the flare evolves. For each flare, the automated routine searches for the optimal set of τ_0, f, and c_0 that produces the best overall correlation and smallest deviations between the model and observed $\mathcal{F}_{\rm sxr}$ during the time period from t_s to t_e.

Figure 3 shows the comparison of the model (thick solid pink) and observed (thick solid black) $\mathcal{F}_{\rm sxr}$ for the 16 flares analyzed in this paper. Also shown in thin solid lines are the total light curve in the AIA 1600 Å passband $\mathcal{F}_{\rm uv}$ (pink) and the time derivative of $\mathcal{F}_{\rm sxr}$ (black). Seen from the figure, the majority of the flares are very well modeled by Equation (1), and the mean difference between the model and observation normalized to the peak of $\mathcal{F}_{\rm sxr}$ is within 10%. Events 14 and 15 are the least successful, suggesting that the flare evolution in these two events may deviate from the general description by Equation (1), particularly in the decay phase. The overall success of this simple model in the majority of the flares suggests that hydrodynamic evolution of flare loops, which contribute to the GOES 1–8 Å SXR emission, may be governed by some general rules (Warren & Antiochos 2004).

Also shown in Figure 3 is the variation of τ_i (green) as the flare evolves. Except for event 4, a growing decay timescale is required to reproduce both the rise and decay of the total SXR emission. Qualitatively, this is consistent with the general observation that, as the flare evolves, reconnection takes place at higher altitudes, forming longer loops, which cool more slowly. Observations show the growing separation of the two ribbons (e.g., Figure 2(a)), evidence for growing loops. However, in a few flares (e.g., flare 5), during the decay of the SXR emission, τ_i becomes much longer than the expected cooling timescales based on observed flare length scales and typical thermodynamic properties of flare loops. Therefore, the empirical decay timescale found here to match the observation is not necessarily the same as the cooling timescale.

We also note that the empirical model (Equation (1)) has also been applied to HXR light curves (in which case, $N = 1$) or the impulsive component of $\mathcal{F}_{{\rm uv},i}$ with its slow-decay component truncated but cannot produce a good agreement with the observed $\mathcal{F}_{\rm sxr}$. These experiments indicate that continuous heating in the gradual phase seems essential in individual loop events and throughout the flare evolution (Qiu & Longcope 2016; Zhu et al. 2018). The empirical model supports the scenario requiring the gradual phase heating in individual loop events, but the model itself is not physical and cannot return the heating rates. To find the amount of energy used in heating the flare corona, we then employ the UFC method to model the evolution of flare loops.

4. Neupert Effect: The UFC Method

The encouraging result from the modified empirical model of the Neupert effect indicates that spatially resolved UV emission may be used as a proxy for heating rates in flare loops. Qiu et al. (2012) and Liu et al. (2013) implemented this idea and developed the UFC method to model flare heating. The method infers heating rates in loop events from the UV light curves at the footpoints and models plasma evolution in these loop events with a zero-dimensional hydrodynamic code, the enthalpy-based thermal evolution of loops model (EBTEL; Klimchuk et al. 2008; Cargill et al. 2012). The UFC method has been applied to analyze and model several flares with varying degrees of success (Qiu et al. 2012; Liu et al. 2013; Zeng et al. 2014; Qiu & Longcope 2016; Zhu et al. 2018). The latest effort by Qiu & Longcope (2016) and Zhu et al. (2018) suggested that, even in one loop event, heating takes place in two phases: an intense impulsive heating phase lasting a few minutes followed by a gradual heating phase lasting up to a few tens of minutes but at a much lower rate. These two phases of heating are reflected in the UV light curve of a single pixel (see Figure 2(b)), usually exhibiting a sharp impulsive rise followed by a long decay. Therefore, in the latest experiment, the UV

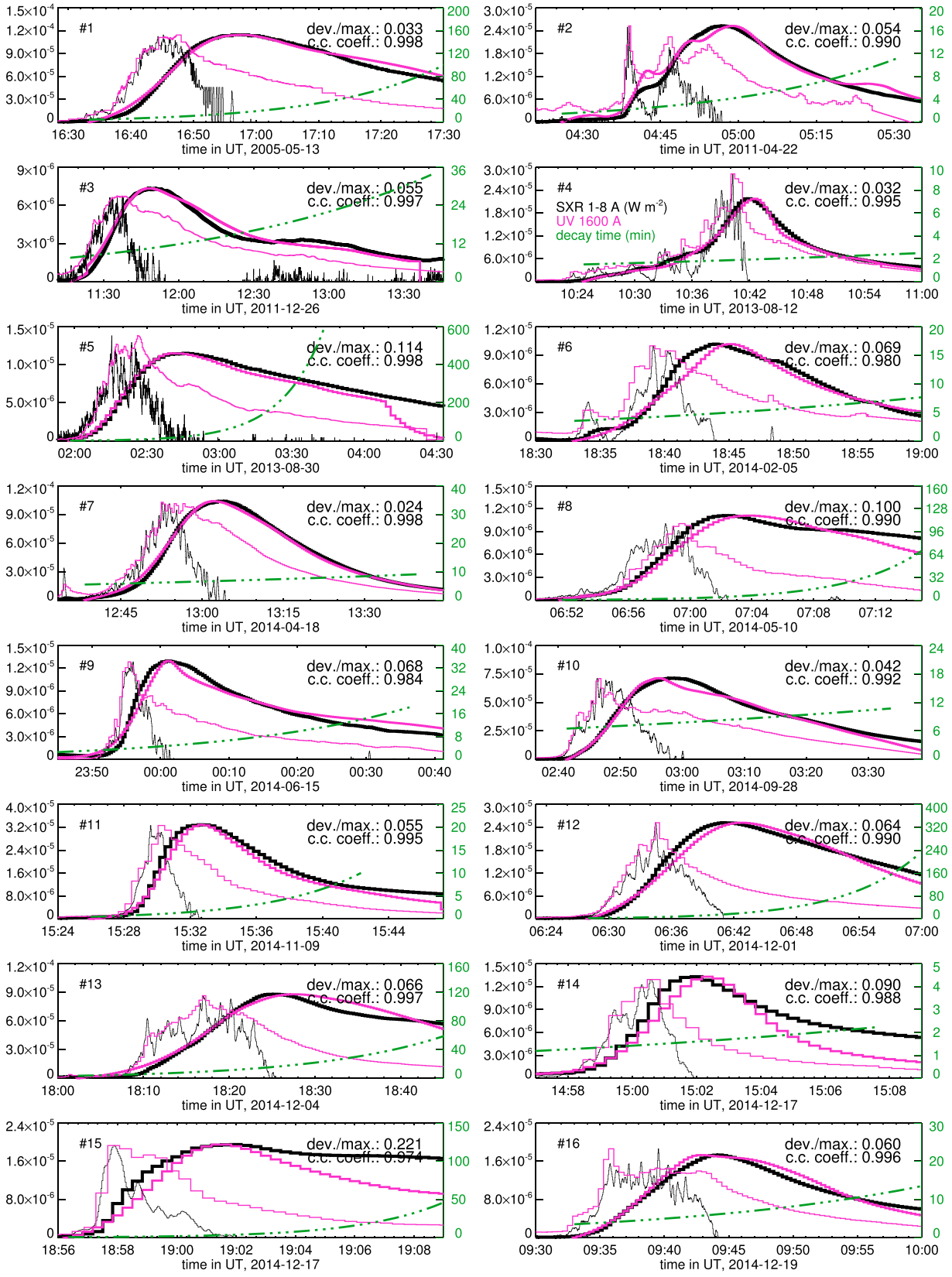

Figure 3. Comparison of the observed SXR "true" flux light curve in 1–8 Å (thick black) with the SXR light curve generated by the empirical model of the Neupert effect (thick pink). Thin curves show the time derivative of the observed SXR light curve (black) and the observed total UV light curve in AIA 1600 Å (pink), both arbitrarily scaled. The green curve shows the time-dependent decay timescale τ_i in minutes (see text). Also marked are the variance (normalized to the observed peak SXR emission) and the coefficient of the cross-correlation between the model and observed SXR light curves.

light curve has been used to infer the heating rate in both the impulsive and gradual phases of heating with which Zhu et al. (2018) successfully modeled a two-ribbon flare with the model synthetic emissions in agreement with the observed emissions in 15 passbands by GOES, AIA, the Extreme-ultraviolet Variability Experiment (EVE; Woods et al. 2012), and the X-ray Telescope (Golub et al. 2007).

In this paper, we use the UFC method to model the 16 flares with a specific focus on understanding the relationship between the UV light curves in the AIA 1600 Å passband and the GOES SXR light curves. The details of the method are given in Qiu et al. (2012) and Liu et al. (2013), with the most recent update by Zhu et al. (2018), which takes into account the two-phase heating, as well as an empirical treatment of thermal conduction suppression (Jiang et al. 2006). In this study, we apply this updated model with the empirical term of turbulent suppression of thermal conduction, which gives rise to higher plasma temperatures at the peak of the flare heating. For simplicity, we do not aim for a full-scale comparison of the model results with multipassband observations, as done before, but rather focus on the GOES SXR light curves at 1–8 and 0.5–4 Å. In addition, we also constrain the cooling rates by comparing the model results with the light curves from the AIA 211 Å passband, which captures flare emission at 2 MK as the plasma cools down. For each flare, we use a scaling constant λ to convert the observed data counts of the UV 1600 Å light curve of a brightened pixel to energy flux in the corresponding loop event: $\mathcal{Q}_i(t)L_i = \lambda\mathcal{F}_{\mathrm{uv},i}(t)$, where $\mathcal{F}_{\mathrm{uv},i}(t)$ is the UV 1600 Å light curve (in units of DN s^{-1} pixel^{-1}), $\mathcal{Q}_i(t)$ is the volumetric heating rate (in units of erg cm^{-3} s^{-1}), and L_i is the length of the half-loop. The length of a given half-loop is $L_i = L_0 + v(t_i - t_s)$, t_i being the time when $\mathcal{F}_{\mathrm{uv},i}(t)$ peaks, and L_0 and the growth rate v are estimated from the time-dependent separation of two newly brightened flare ribbons in the positive and negative magnetic fields, assuming that the half-loop is a quarter of a circle whose diameter is the mean distance between two flare ribbons. With these heating rates as input, and another free parameter η that describes the radiative loss from the transition region as scaled to the mean pressure in the flare loop (Qiu et al. 2013), the model computes the mean temperature and density of thousands of loop events that evolve with time, and the resultant time-dependent differential emission measure is convolved with the emissivity and instrument response functions.[2] For a given flare, λ and η are constant for all of the identified loop events; for different flares, λ and η may be different. We model each flare with varying λ and η and find the optimal values that give the best comparison between the observed and synthetic GOES SXR fluxes at two channels and EUV flux at the AIA 211 Å passband.

Figure 4 shows the comparison of the observed and model synthetic SXR and EUV fluxes for the 16 flares. In each panel, the synthetic SXR light curves in 1–8 (thick solid pink) and 0.5–4 (thin solid pink) Å and EUV 211 Å light curve (dashed green) are the average from two model runs conducted with different λ and η values that produce the optimal comparison with the observed SXRs (solid black) and EUV 211 Å flux (solid green). The total heating rate (blue) is also the average of the two runs. For clarity of the display, the synthetic and observed GOES SXR flux in 0.5–4 Å is multiplied by a factor of 2, and uncertainties, which are small fractions of the mean fluxes, are not plotted in the figure. Seen in the figure, in the majority of the flares, the synthetic SXR and EUV fluxes are in reasonable agreement with the observed fluxes.

Note that the zero-dimensional model is not capable of accurately calculating plasma properties out of equilibrium during the very dynamic heating phase in the first few minutes; therefore, the model cannot produce sufficient SXR 0.5–4 Å emission at very high temperatures, which is likely the case in a few flares, like event 11. Nevertheless, the total SXR 1–8 Å and EUV emissions summed over all loops during the flare timescale are mostly produced at lower temperatures, and they greatly depend on the total energy deposit in the loops and are less subject to the details of heating and plasma evolution in nonequilibrium in the short impulsive heating phase (see discussions by Winebarger & Warren 2004). Therefore, the overall agreeable comparison between the synthetic and observed total fluxes suggests that the heating rates inferred from the flare footpoint UV 1600 Å emissions are reasonable first-order estimates. It is noted, though, that in the decay phase of a number of flares, the model does not produce sufficient $\mathcal{F}_{\mathrm{sxr}}$ emission as observed. This will be further discussed in the next section, in conjunction with the result of the empirical Neupert model.

We recall that the profile of the heating rate for each loop event used in the model resembles the time profile of the UV light curve at the foot, which generally consists of an impulsive component followed by a gradual component (see Figure 2). As a comparison, the dashed pink curves in Figure 4 show the synthetic $\mathcal{F}_{\mathrm{sxr}}$ in 1–8 Å with the impulsive heating model. For the impulsive model, the heating rate of a loop event is derived by fitting the rise of the UV light curve to a half Gaussian, and the impulsive heating rate is a full Gaussian (Qiu et al. 2012; Liu et al. 2013). All other properties, such as the lengths of the loop events, are the same in the impulsive and two-phase heating models. The figure shows that, in the majority of the flares, the two-phase heating model produces synthetic SXR emission in much better agreement with the observed SXR emission than the model only using impulsive heating rates. The necessity of two-phase heating requires a greater amount of flare heating energy than the impulsive heating. In different flares, the fraction of impulsive heating energy out of the total varies from 40% to 85%; on average, the amount of heating energy in the impulsive components takes up about two-thirds of the total heating energy, and the remaining one-third of the heating energy is distributed in the gradual components of the heating events.

5. Energetics of Flare Heating

5.1. Estimate of Flare Heating Energy

The UFC method allows us to estimate the total energy deposit in the flare corona. However, in a number of flares, the model still does not produce sufficient SXR emission in the decay phase; therefore, the total heating energy derived directly from the UFC method is likely the lower limit of the corona heating energy. On the other hand, $\mathcal{F}_{\mathrm{sxr}}$ produced by the empirical model compares better with the observation in the decay phase; yet the empirical model only relates the time

[2] The GOES response function is derived with the SSWIDL code goes_fluxes.pro, and the response functions for the AIA EUV passbands are derived with aia_get_response.pro. These response functions are provided by the instrument teams using the latest calibration, as of 2020 October, with the CHIANTI 9.0.1 atomic database and coronal abundance. The AIA response functions are also calibrated with EVE.

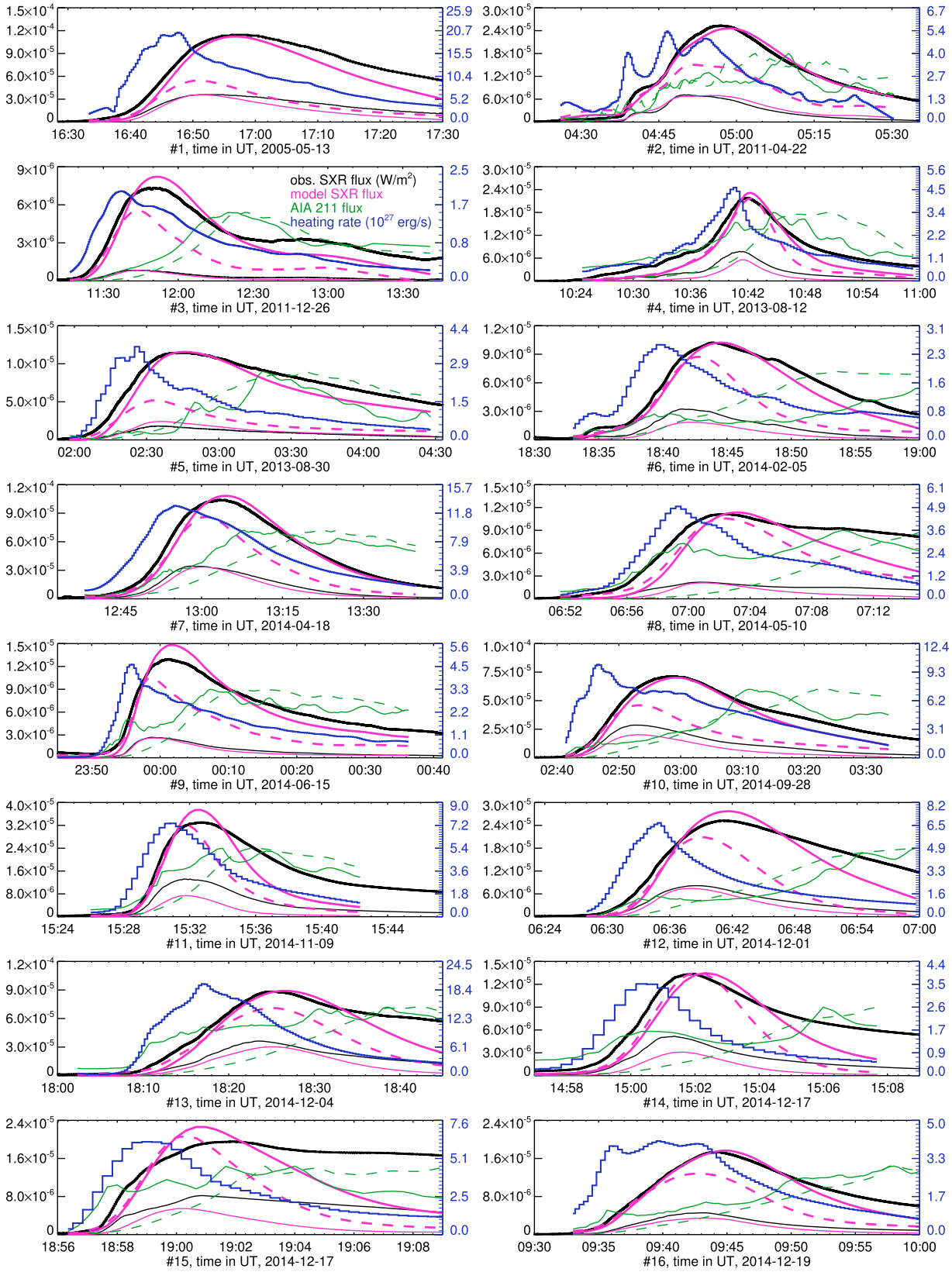

Figure 4. Comparison of the GOES observed SXR light curves in 1–8 Å (thick black), 0.5–4 Å (thin black), and the AIA-observed EUV flux at 211 Å passband (solid green) with the synthetic SXRs (thick and thin solid pink) and EUV (dashed green) light curves by the UFC method that includes gradual heating. For comparison, the SXR 1–8 Å light curve by the UFC method using only impulsive heating is shown in dashed pink. Also plotted in each panel is the total heating rate (blue) derived from the UFC method. The AIA 211 Å light curves are arbitrarily scaled. For clarity of the display, uncertainties in the synthetic SXR and EUV light curves and heating rates are not plotted, but they are described in the text (Section 4).

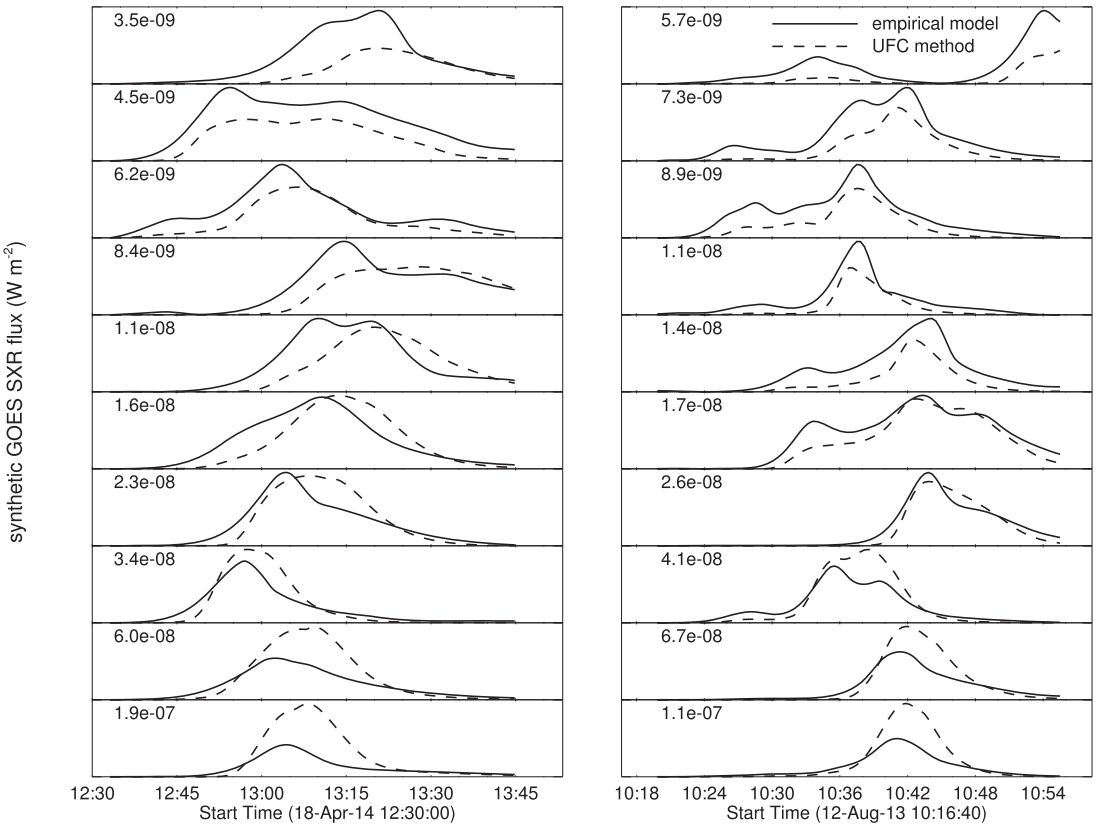

Figure 5. Left: synthetic SXR light curves in 1–8 Å with the empirical model (solid) and UFC method (dashed) in 10 randomly sampled loop events for the flare SOL 2014-04-18. Right: same as the left panels but for the flare SOL 2013-08-12. Marked in each panel is the peak flux of the SXR light curve by the UFC method.

evolution of flare SXR and UV 1600 Å emission and cannot return the heating rates. To help improve estimates of heating energies, we may use the results from the empirical model to calibrate heating energies derived from the UFC method.

To understand the difference in the total SXR flux produced by the two models, we compare the synthetic SXR flux in individual loop events. Figure 5 shows the synthetic SXR light curves in 10 randomly sampled loop events generated by the empirical model (solid) and UFC method (dashed), respectively, for the two flares displayed in Figure 2. It is seen that the SXR fluxes generated by the two models have very similar time profiles, yet for weak events, the magnitude of the SXR flux by the UFC method is lower than that by the empirical model. Such a comparison may explain the insufficient SXR emission by the UFC method during the decay of the flare, when flare heating and the SXR flux in individual loop events become smaller. Since the empirical model is able to produce the total SXR flux that compares better with the observation, we will assume that the SXR emission in each loop event generated by the empirical model represents the ground truth and uses it to make new estimates of heating energies in flare loops.

For this purpose, we first establish the relation between the heating energy and the synthetic GOES SXR emission by the UFC-EBTEL model. The left panel of Figure 6 shows a scatter plot of the time-integrated heating energy in the loops, denoted as $\mathcal{E}_{\rm UFC}$ (in units of erg), versus the time-integrated synthetic GOES SXR flux generated by the EBTEL model, denoted as $\mathcal{G}_{\rm UFC}$ (in units of J m^{-2}). The $\mathcal{E}$–$\mathcal{G}$ scatter plot is quite tight for each flare and can be described by a power law $\mathcal{E} \approx 10^{\beta}\mathcal{G}^{\alpha}$. For the flares modeled in this event, α ranges between 0.45 and 0.67, and β ranges from 29.52 to 30.56. In fact, the $\mathcal{E}$–$\mathcal{G}$ relation for all loop events in all 16 flares can be fitted to one power law, as shown in the figure (solid black line), yielding $\langle\alpha\rangle = 0.535 \pm 0.001$ and $\langle\beta\rangle = 29.990 \pm 0.004$. This scaling law allows us, without running the hydrodynamic model, to estimate the total SXR emission in a loop event given the amount of the heating energy, and vice versa.

In comparison, the right panel of Figure 6 shows the time-integrated synthetic SXR emission generated by the empirical model $\mathcal{G}_{\rm emp}$; for a better comparison, we exclude events 14 and 15, which are not well modeled with the empirical formula. As expected, $\mathcal{G}_{\rm UFC}$ becomes increasingly underestimated for smaller $\mathcal{G}_{\rm emp}$. Based on these analyses, we make a new estimate of flare heating energy, denoted as $\mathcal{E}_{\rm emp}$, using $\mathcal{G}_{\rm emp}$ as the ground truth for the SXR emission by each loop event to replace $\mathcal{G}_{\rm UFC}$ in the $\mathcal{E}$–$\mathcal{G}$ scaling, namely, $\mathcal{E}_{\rm emp} \approx 10^{\beta}\mathcal{G}_{\rm emp}^{\alpha}$. The estimate can be made using α and β derived for each flare or $\langle\alpha\rangle$ and $\langle\beta\rangle$ derived for all flares, and the difference in the estimate is not found to be significant. We take the average $\mathcal{E}_{\rm emp}$ from these two estimates as a plausible upper limit of the heating energy in each loop event, whereas the heating energy $\mathcal{E}_{\rm UFC}$ derived from the original UFC method is taken as the lower limit.

Figure 7(a) shows the distribution of heating energies $\mathcal{E}$, the mean of $\mathcal{E}_{\rm emp}$ and $\mathcal{E}_{\rm UFC}$. The new estimate changes the distribution of heating energies in the loop events, which becomes tighter toward higher energies, and raises the total

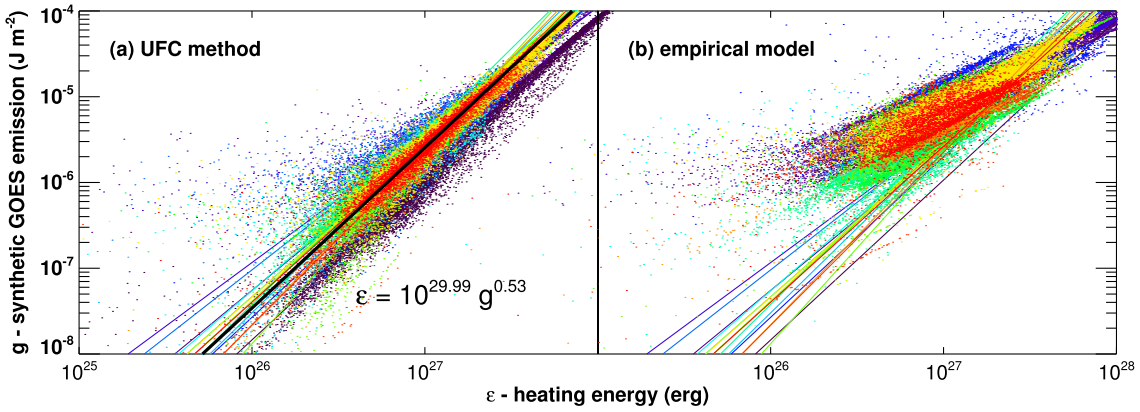

Figure 6. Scatter plot of the time-integrated SXR flux in 1–8 Å $\mathcal{G}$ generated by the UFC method (a) or the empirical Neupert model (b) against the total heating energy $\mathcal{E}_{\rm UFC}$ in individual loops. Each color shows a few thousand loop events for a given flare, and the solid line of the same color illustrates the $\mathcal{E}_{\rm UFC} - \mathcal{G}_{\rm UFC}$ fit to a power law for the same flare. The black solid line shows the $\mathcal{E}_{\rm UFC} - \mathcal{G}_{\rm UFC}$ fit to a power law for all loop events in all 16 flares. Note that the solid colored lines in panel (b) are the same as in panel (a) for comparison of the synthetic SXR emissions generated by the two models.

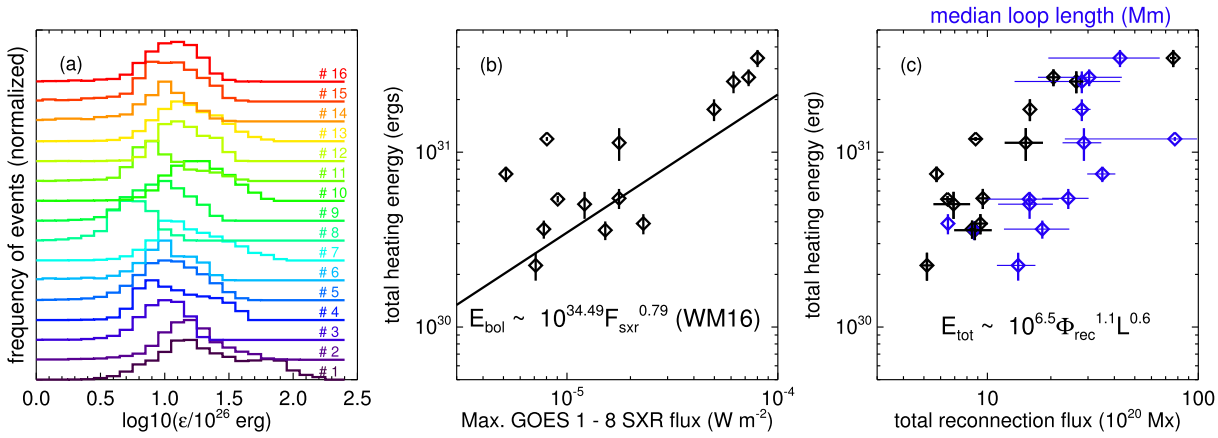

Figure 7. (a) Histograms of the heating energies in the loop events for each of the 16 flares analyzed in the paper. Here the heating energy in each loop event is the average of $\mathcal{E}_{\rm UFC}$ and $\mathcal{E}_{\rm emp}$. (b) Scatter plot of the total heating energy against the magnitude of the flare (based on the "scaled" flux). Vertical bars indicate the range of the total heating energy, with $\sum\mathcal{E}_{\rm UFC}$ being the lower limit and $\sum\mathcal{E}_{\rm emp}$ being the upper limit. The solid guide line shows the power-law scaling of the observed bolometric radiation energy to the flare magnitude given by Warmuth & Mann (2016). (c) Total heating energy against the reconnection flux $\Phi_{\rm rec}$ (black; see text) and median length L of the flare loop events (blue). Vertical bars indicate the ranges of the flare heating energy, as in panel (b); horizontal bars indicate the uncertainties of the $\Phi_{\rm rec}$ measurements (black) or the standard deviations of the estimated lengths (blue) of the loop events that are subsequently formed during the flare evolution from rise to decay.

flare heating energy by one-third, on average. Panel (b) shows the total energy $\mathcal{E}_{\rm tot} = \sum\mathcal{E}$ (in erg) that is used to heat the flare corona for each of the 14 flares (i.e., excluding events 14 and 15) plotted against the flare magnitude defined by the peak SXR flux in the GOES 1–8 Å channel.[3] Each vertical bar indicates the range of the total heating energy, the lower limit being the sum of $\mathcal{E}_{\rm UFC}$ and the upper limit the sum of $\mathcal{E}_{\rm emp}$, and the symbols indicate $\mathcal{E}_{\rm tot}$, the mean of $\sum\mathcal{E}_{\rm UFC}$ and $\sum\mathcal{E}_{\rm emp}$. Overplotted is the scaling law by Warmuth & Mann (2016, WM16 scaling law hereafter) that relates the total (bolometric) radiation energy of flares observed between 1996 and 2007 (Kretzschmar 2011; Emslie et al. 2012) to their GOES magnitude: $\mathcal{E}_{\rm bol} \approx 10^{34.49\pm0.44}\mathcal{F}_{\rm sxr}^{0.79\pm0.10}$. The total heating energy derived in this study scatters around the WM16 scaling law,[4] suggesting that this study has achieved a close estimate of the total heating energy in flares. Warmuth & Mann (2016) also derived the maximum thermal energy $\mathcal{E}_{\rm th}$ and nonthermal electron energy $\mathcal{E}_{n\rm th}$ of 24 flares observed by GOES and RHESSI between 2002 and 2003, which scale with the flare magnitude as $\mathcal{E}_{\rm th} \approx 10^{33.67\pm0.26}\mathcal{F}_{\rm sxr}^{0.88\pm0.06}$ and $\mathcal{E}_{n\rm th} \approx 10^{35.07\pm0.38}\mathcal{F}_{\rm sxr}^{1.08\pm0.09}$, respectively. The heating energy estimated here is nearly an order of magnitude larger than the maximum thermal energy and is also greater than the nonthermal electron energy, particularly in small flares. Therefore, flare heating is not entirely due to nonthermal electrons, and the footpoint UV emission signatures more comprehensively capture heating events during the flare regardless of heating mechanisms.

5.2. Reconnection and Energetics

Magnetic reconnection forms flare loops and releases energy that is used to heat them. The amount of magnetic flux $\Phi_{\rm rec}$ participating in reconnection is measured by summing up the magnetic flux in the pixels (see Figures 2(a) and (c)) whose brightness in the 1600 Å passband is increased to be more than four times the quiescent brightness and for at least 4 minutes. Flares in this study take place near the disk center, and we

[3] Here, to be consistent with prior literature, the flare magnitude is derived with the "scaled" GOES SXR flux but not the "true" flux. The "true" flux in this channel, as released in 2020 October, is equivalent to the "scaled" flux divided by 0.7 (https://hesperia.gsfc.nasa.gov/rhessidatacenter/complementary_data/goes.html).

[4] The energy–magnitude scaling in this study is $\mathcal{E}_{\rm tot} \approx 10^{34.33\pm0.81}\mathcal{F}_{\rm sxr}^{0.72\pm0.17}$.

integrate the HMI-measured longitudinal photospheric magnetic flux density B (in units of Gauss, or Mx cm^{-2}) in flaring pixels without correcting the projection effect or extrapolating B to the upper chromosphere or transition region, since these two effects partly cancel each other out. Finally, the measurement assumes that each patch of magnetic flux anchored at a UV-brightened pixel participates in magnetic reconnection only once to form a flare loop containing this flux. The uncertainty is estimated from $\Phi_{\rm rec}$ measured in the positive and negative magnetic fields, which, on average, is about 20% of $\Phi_{\rm rec}$ (also see Qiu & Yurchyshyn 2005; Qiu et al. 2007).

Figure 1 shows the reconnection rate $\dot{\Phi}_{\rm rec}$, the time derivative of the time-dependent reconnection flux, which varies in the range of 10^{17-19} Mx s^{-1} from flare to flare. The figure shows that $\dot{\Phi}_{\rm rec}$ is more impulsive and usually precedes the total heating rate $\dot{\mathcal{E}}_{\rm tot}$. In most flares, $\dot{\Phi}_{\rm rec}$ does not diminish to zero after the peak of the SXR emission, indicating that reconnection and formation of new flare loops continues into the decay phase, although at a much smaller reconnection rate and with the amount of reconnection flux making only a small fraction of the total reconnection flux. On the other hand, the analysis of energetics in Section 5.1 suggests that the total heating energy in the decay phase of the flare is nonnegligible, amounting to 27%, on average.

These observations imply that the heating energy $\mathcal{E}$ in individual loop events is not a simple linear function of the magnetic flux in the loop, and loop events in the early phase of the flare have less energy per unit flux compared with loop events in the later phase of the flare. A regression analysis yields a very weak dependence of the heating energy $\mathcal{E}$ on either the magnetic flux or the length of the loop events. On the other hand, the integrated total energy of the flare exhibits a much stronger dependence on the reconnection flux, $\mathcal{E}_{\rm tot} \sim \Phi_{\rm rec}^{1.1\pm0.2} L^{0.6\pm0.1}$, as shown in Figure 7(c).[5] Here L is the median length of the loop events in units of megameters. The energy dependence on $\Phi_{\rm rec}$ is very close to that found by Reep & Knizhnik (2019) and Zhu et al. (2018). Reep & Knizhnik (2019) analyzed a few thousand flares, and the energy in the scaling law refers to the flare thermal energy at the time of peak temperature, deduced from GOES SXR observations. Zhu et al. (2018) analyzed only one event, SOL 2011-12-16 (event 3), and the flux energy patches are grouped into a few tens of magnetic cells to construct the scaling law. Zhu et al. (2018) did not reveal a dependence on the loop length, which does not vary significantly during this flare. In a somewhat different context, Schrijver et al. (2004) found a similar scaling law, $\mathcal{F}_H \sim \langle B \rangle^{1.0\pm0.3} L^{-1.0\pm0.5}$, that relates the heating flux $\mathcal{F}_H$ (in units of erg cm^{-2} s^{-1}) of active regions to the mean magnetic field strength $\langle B \rangle$ at the base (the chromosphere) and the scale size L of the active region loops. We may rewrite their scaling law as $\mathcal{E}_{\rm tot} \sim \mathcal{F}_H A \tau \sim \Phi^{1.0} L^{1.0}$, considering that the magnetic flux is given by $\Phi = \langle B \rangle A$, A being the total cross-sectional area of active region loops, and, in equilibrium, the heating timescale is roughly the same as the thermal conduction timescale $\tau \sim L^2$. On global scales ranging from active regions to magnetic cells in a given active region and within the uncertainties, these scaling laws are very similar; in particular, the energy dependence on the magnetic field is the same, indicating the similar nature of the energy release in these systems (Schrijver et al. 2004).

[5] Note that this scaling law is derived for the 13 flares observed by AIA and HMI, excluding events 1, 14, and 15. Scaling laws involving magnetic field measurements change significantly when the first event is included. With this event included, the energy–flux relation becomes $\mathcal{E}_{\rm tot} \sim \Phi_{\rm rec}^{0.8\pm0.1} L^{0.6\pm0.2}$. In addition, the scaling of the flare magnitude and reconnection flux is found to be $\mathcal{F}_{\rm sxr} \sim \Phi_{\rm rec}^{1.6\pm0.2}$ for the 13 flares, similar to that in Kazachenko et al. (2017), who analyzed more than 3000 flares observed by AIA and HMI and found $\mathcal{F}_{\rm sxr} \sim \Phi_{\rm rec}^{1.5}$; with the first event included, the magnitude–flux scaling in this study becomes $\mathcal{F}_{\rm sxr} \sim \Phi_{\rm rec}^{1.1\pm0.2}$. The first event was observed by TRACE and MDI, so the discrepancy might be due to different calibrations of the two generations of instruments.

6. Conclusions and Discussions

6.1. Summary

In this study, we estimate the total energy that is used to heat flare plasmas in the corona using two simplified models, an empirical model of the Neupert effect and a zero-dimensional hydrodynamic model (the UFC method). The purpose of the study is to derive a first-order estimate of flare energies in a multitude of flare loops. Although these models are incapable of precisely describing thermodynamic properties during the initial impulsive heating phase of a flare loop when nonequilibrium physics governs the loop evolution, they are suitable for the thought experiment, as conducted in this paper, on the long-standing perception that energy release and flare heating take place in numerous patches over an extended time period. The experiment takes advantage of spatially resolved UV emission from the footpoints of flare loops at the transition region or upper chromosphere, assuming that each UV-brightened pixel represents a single patch of energy release, denoted as a loop event or heating event in this study. The experiment extends the traditional concept of the Neupert effect to spatially resolved UV light curves.

We have conducted the experiment on 16 flares ranging from C to M class. The study confirms that a multitude of impulsive heating events alone cannot reproduce the observed flare SXR light curve, but the two-phase heating model produces the synthetic SXR emission in better agreement with observations. This is consistent with the recent finding by Kerr et al. (2020), who conducted one-dimensional loop simulations with impulsive heating at fine scales and found that the model-produced thermodynamic properties decay faster than observed by IRIS. Furthermore, comparing the empirical model of the UV Neupert effect and the UFC method, the former producing the SXR emission in the decay phase in still better agreement with observations than the latter, we have improved the estimate of the flare heating energy, particularly in the decay phase of the flare; on average, the amount of heating energy in the decay phase of the flare (i.e., after the peak of the total SXR emission in 1–8 Å) makes up 27% of the total heating energy during the flare.

The estimated energies used to heat the flare corona are comparable with the bolometric radiation energy measured in flares of similar magnitudes (Warmuth & Mann 2016). Therefore, the UV emission signatures at the footpoints of flare loops well capture heating events during the flare regardless of heating mechanisms. The flare heating energy $\mathcal{E}_{\rm tot}$ is also shown to scale with the total reconnection flux $\Phi_{\rm rec}$ and the median length of the flare half-loops L by $\mathcal{E}_{\rm tot} \sim \Phi_{\rm rec}^{1.1\pm0.2} L^{0.6\pm0.1}$; the dependence of the heating energy on the magnetic field is similar to scaling laws found in some studies, though with various contexts (Schrijver et al. 2004; Zhu et al. 2018; Reep & Knizhnik 2019), but different from some other studies, such as those by Aschwanden (2020a, 2020b, and references therein). On the other hand, we do not find a strong dependence of the heating energy on the

magnetic field (flux) and/or the loop length for individual loop events down to the pixel scale (~0.″6).

6.2. Discussions

Numerous prior studies have examined scaling laws that relate the flare magnitude, namely, the peak GOES SXR flux in 1–8 Å, to flare energies of various kinds. Some of these studies also take into account the length scale of the flare loops. Based on the Rosner–Tucker–Vaiana (RTV) scaling law, Warren & Antiochos (2004) found the flux–energy relation to be superlinear, $\mathcal{F}_{\rm sxr} \sim \mathcal{E}_{\rm tot}^{1.75} L^{-1}$ (here $\mathcal{F}_{\rm sxr}$ refers to the peak SXR flux in units of W m^{-2}), which was confirmed with a one-dimensional hydrodynamic model of loop heating by a beam of nonthermal electrons. One-dimensional loop simulations by Reep et al. (2013) yielded a similar scaling law, $\mathcal{F}_{\rm sxr} \sim \mathcal{E}_{\rm tot}^{1.7}$. However, analyzing a few thousand flares using the database by Kazachenko et al. (2017), Reep & Knizhnik (2019) found sublinear scaling laws $\mathcal{F}_{\rm sxr} \sim \mathcal{E}_{\rm th}^{0.85}$ and $\mathcal{E}_{\rm tot}^{0.85}$, the former referring to the thermal energy of the flare (at the time of peak temperature) derived from the GOES SXR analysis and the latter referring to the flare heating energy deduced from the traditional Neupert effect, i.e., $\mathcal{E}_{\rm tot}$ being the nonthermal electron energy. Similarly, Aschwanden (2020c) found $\mathcal{F}_{\rm sxr} \sim \mathcal{E}_{\rm diss}^{0.7}$, where $\mathcal{E}_{\rm diss}$ refers to energy dissipated in flares. Finally, the scaling laws by Warmuth & Mann (2016) would suggest $\mathcal{F}_{\rm sxr} \sim \mathcal{E}_{\rm bol}^{1.3}$, $\mathcal{E}_{\rm nth}^{0.9}$, and $\mathcal{E}_{\rm th}^{1.1}$.

From this study, we find a superlinear flux–energy relation, $\mathcal{F}_{\rm sxr} \sim \mathcal{E}_{\rm tot}^{1.4\pm0.2} L^{-1.1\pm0.2}$, for 14 flares (excluding events 14 and 15, which are not well modeled); again, the flux–energy dependence is closest to the WM16 scaling law of the bolometric energy. The difference from the other scaling laws by, e.g., Warren & Antiochos (2004), Reep et al. (2013), Reep & Knizhnik (2019), and Aschwanden (2020c) may be due to the fact that flare heating takes place over an extended time period beyond the impulsive phase and is not provided only by nonthermal electrons.

The modified empirical model of the UV Neupert effect is able to produce SXR light curves in very good agreement with observations, which is used, in this study, to return an improved estimate of flare energetics, particularly in the decay phase. However, we do not fully understand the implication of the convolution in the form of a Gaussian (Equation (1)) with a decay timescale that becomes very large at times. Guided by this thought experiment, in future work, we will investigate the physical reason for the discrepancy between the two models and then conduct a full-scale modeling of flare evolution with the improved UFC method employing multiple-wavelength observations in a larger number of flares (Zhu C. et al. 2021, in preparation). This study may also serve as a prior experiment for more comprehensive and physics-based models, which can unravel the physics of heating mechanisms (Longcope & Klimchuk 2015; Kowalski et al. 2019; Reep et al. 2019; Graham et al. 2020; Kerr et al. 2020) and also help address production of flare UV emissions in the transition region and upper chromosphere (e.g., McClymont & Canfield 1986; Milligan 2015; Simões et al. 2019), used in this study as a proxy for heating.

The author thanks the referee for constructive comments that help improve the analysis and clarity of the manuscript. The author thanks Lilly Bralts-Kelly and Jianxia Cheng for helping prepare the AIA data. This work has been supported by NASA grants NNX14AC06G and 80NSSC19K0269. The work also benefits from the ISSI/ISSI-BJ team collaboration "Diagnosing Heating Mechanisms in Solar Flares." SDO is a mission of NASA's Living With a Star Program.

ORCID iDs

Jiong Qiu https://orcid.org/0000-0002-2797-744X

References

Alexander, D., & Coyner, A. J. 2006, ApJ, 640, 505
Antonucci, E., Gabriel, A. H., Acton, L. W., et al. 1982, SoPh, 78, 107
Aschwanden, M. J. 2020a, ApJ, 895, 134
Aschwanden, M. J. 2020b, ApJ, 903, 23
Aschwanden, M. J. 2020c, ApJ, 897, 16
Aschwanden, M. J., & Alexander, D. 2001, SoPh, 204, 91
Aschwanden, M. J., Caspi, A., Cohen, C. M. S., et al. 2017, ApJ, 836, 17
Cargill, P. J., Bradshaw, S. J., & Klimchuk, J. A. 2012, ApJ, 758, 5
Cheng, C.-C. 1990, ApJ, 349, 362
Cheng, C. C., Tandberg-Hanssen, E., & Orwig, L. E. 1984, ApJ, 278, 853
Cheng, C.-C., Vanderveen, K., Orwig, L. E., & Tand Berg-Hanssen, E. 1988, ApJ, 330, 480
Cheng, J. X., Kerr, G., & Qiu, J. 2012, ApJ, 744, 48
Coyner, A. J., & Alexander, D. 2009, ApJ, 705, 554
Culhane, J. L., Hiei, E., Doschek, G. A., et al. 1991, SoPh, 136, 89
Dennis, B. R., & Zarro, D. M. 1993, SoPh, 146, 177
Dere, K. P., & Cook, J. W. 1979, ApJ, 229, 772
Effenberger, F., Rubio da Costa, F., Oka, M., et al. 2017, ApJ, 835, 124
Emslie, A. G., Dennis, B. R., Shih, A. Y., et al. 2012, ApJ, 759, 71
Emslie, A. G., Li, P., & Mariska, J. T. 1992, ApJ, 399, 714
Fisher, G. H., Canfield, R. C., & McClymont, A. N. 1985, ApJ, 289, 425
Fisher, G. H., & Hawley, S. L. 1990, ApJ, 357, 243
Fletcher, L., Dennis, B. R., Hudson, H. S., et al. 2011, SSRv, 159, 19
Fletcher, L., & Hudson, H. 2001, SoPh, 204, 69
Fletcher, L., & Hudson, H. S. 2008, ApJ, 675, 1645
Gan, W. Q., Zhang, H. Q., & Fang, C. 1991, A&A, 241, 618
Glesener, L., Krucker, S., Duncan, J., et al. 2020, ApJL, 891, L34
Golub, L., Deluca, E., Austin, G., et al. 2007, SoPh, 243, 63
Graham, D. R., & Cauzzi, G. 2015, ApJL, 807, L22
Graham, D. R., Cauzzi, G., Zangrilli, L., et al. 2020, ApJ, 895, 6
Grefenstette, B. W., Glesener, L., Krucker, S., et al. 2016, ApJ, 826, 20
Jiang, Y. W., Liu, S., Liu, W., & Petrosian, V. 2006, ApJ, 638, 1140
Kane, S. R., & Donnelly, R. F. 1971, ApJ, 164, 151
Kazachenko, M. D., Lynch, B. J., Welsch, B. T., & Sun, X. 2017, ApJ, 845, 49
Kerr, G. S., Allred, J. C., & Polito, V. 2020, ApJ, 900, 18
Kerr, G. S., Fletcher, L., Russell, A. e. J. B., & Allred, J. C. 2016, ApJ, 827, 101
Klimchuk, J. A., Patsourakos, S., & Cargill, P. J. 2008, ApJ, 682, 1351
Kosugi, T., Makishima, K., Murakami, T., et al. 1991, SoPh, 136, 17
Kowalski, A. F., Butler, E., Daw, A. N., et al. 2019, ApJ, 878, 135
Kretzschmar, M. 2011, A&A, 530, A84
Lee, T. T., Petrosian, V., & McTiernan, J. M. 1995, ApJ, 448, 915
Lemen, J. R., Title, A. M., Akin, D. J., et al. 2012, SoPh, 275, 17
Li, P., Emslie, A. G., & Mariska, J. T. 1993, ApJ, 417, 313
Lin, R. P., Dennis, B. R., Hurford, G. J., et al. 2002, SoPh, 210, 3
Liu, W.-J., Qiu, J., Longcope, D. W., & Caspi, A. 2013, ApJ, 770, 111
Longcope, D. W. 2014, ApJ, 795, 10
Longcope, D. W., & Klimchuk, J. A. 2015, ApJ, 813, 131
Mariska, J. T., Emslie, A. G., & Li, P. 1989, ApJ, 341, 1067
McAteer, R. T. J., & Bloomfield, D. S. 2013, ApJ, 776, 66
McClymont, A. N., & Canfield, R. C. 1986, ApJ, 305, 936
McTiernan, J. M., Fisher, G. H., & Li, P. 1999, ApJ, 514, 472
Milligan, R. O. 2015, SoPh, 290, 3399
Nagai, F., & Emslie, A. G. 1984, ApJ, 279, 896
Neupert, W. M. 1968, ApJL, 153, L59
Orwig, L. E., Frost, K. J., & Dennis, B. R. 1980, SoPh, 65, 25
Pesnell, W. D., Thompson, B. J., & Chamberlin, P. C. 2012, SoPh, 275, 3
Qiu, J., Hu, Q., Howard, T. A., & Yurchyshyn, V. B. 2007, ApJ, 659, 758
Qiu, J., Liu, C., Gary, D. E., Nita, G. M., & Wang, H. 2004a, ApJ, 612, 530
Qiu, J., Liu, W., Hill, N., & Kazachenko, M. 2010, ApJ, 725, 319
Qiu, J., Liu, W.-J., & Longcope, D. W. 2012, ApJ, 752, 124
Qiu, J., & Longcope, D. W. 2016, ApJ, 820, 14
Qiu, J., Sturrock, Z., Longcope, D. W., Klimchuk, J. A., & Liu, W.-J. 2013, ApJ, 774, 14
Qiu, J., Wang, H., Cheng, C. Z., & Gary, D. E. 2004b, ApJ, 604, 900
Qiu, J., & Yurchyshyn, V. B. 2005, ApJL, 634, L121
Reep, J. 2014, PhD thesis, Rice University

Reep, J. W., Bradshaw, S. J., Crump, N. A., & Warren, H. P. 2019, ApJ, 871, 18
Reep, J. W., Bradshaw, S. J., & McAteer, R. T. J. 2013, ApJ, 778, 76
Reep, J. W., & Knizhnik, K. J. 2019, ApJ, 874, 157
Rubio da Costa, F., Kleint, L., Petrosian, V., Liu, W., & Allred, J. C. 2016, ApJ, 827, 38
Ryan, D. F., Chamberlin, P. C., Milligan, R. O., & Gallagher, P. T. 2013, ApJ, 778, 68
Saba, J. L. R., Gaeng, T., & Tarbell, T. D. 2006, ApJ, 641, 1197
Schou, J., Scherrer, P. H., Bush, R. I., et al. 2012, SoPh, 275, 229
Schrijver, C. J., Sandman, A. W., Aschwand EN, M. J., & De Rosa, M. L. 2004, ApJ, 615, 512
Schwartz, R. A., Dennis, B. R., Fishman, G. J., et al. 1992, NASA Conference Publication, 3137, 457
Simões, P. J. A., Reid, H. A. S., Milligan, R. O., & Fletcher, L. 2019, ApJ, 870, 114
Somov, B. V., Syrovatskii, S. I., & Spektor, A. R. 1981, SoPh, 73, 145
Tsuneta, S., Acton, L., Bruner, M., et al. 1991, SoPh, 136, 37
Veronig, A., Vršnak, B., Dennis, B. R., et al. 2002, A&A, 392, 699
Veronig, A. M., Brown, J. C., Dennis, B. R., et al. 2005, ApJ, 621, 482
Warmuth, A., & Mann, G. 2016, A&A, 588, A116
Warren, H. P., & Antiochos, S. K. 2004, ApJL, 611, L49
Warren, H. P., & Warshall, A. D. 2001, ApJL, 560, L87
Winebarger, A. R., & Warren, H. P. 2004, ApJL, 610, L129
Withbroe, G. L. 1978, ApJ, 225, 641
Woods, T. N., Eparvier, F. G., Hock, R., et al. 2012, SoPh, 275, 115
Zeng, Z., Qiu, J., Cao, W., & Judge, P. G. 2014, ApJ, 793, 87
Zhu, C., Qiu, J., & Longcope, D. W. 2018, ApJ, 856, 27